SCIENTIFIC REPORTS

OPEN

Effect of Nb concentration on the spin-orbit coupling strength in Nb-doped SrTiO$_3$ epitaxial thin films

Seong Won Cho[1,2], Milim Lee[1], Sungmin Woo[3], Kanghoon Yim [4], Seungwu Han[4], Woo Seok Choi[3] & Suyoun Lee[1,2]

Several oxide materials have attracted much interest for the application in spintronic devices due to unusual properties originating from the strongly correlated orbital and spin degrees of freedom. One missing part in *oxide spintronics* is a good spin channel featured by strong spin-orbit coupling (SOC) which enables an efficient control of the electron's spin. We have systematically investigated the dependence of the SOC strength of Sr(Nb$_x$Ti$_{1−x}$)O$_3$ thin films on Nb concentration (n_{Nb} = 2~20 at. %) as a deeper exploration of a recent finding of the strong SOC in a heavily Nb-doped SrTiO$_3$ (Sr(Nb$_{0.2}$Ti$_{0.8}$)O$_3$) epitaxial film. Apart from a finding of a proportionality of the SOC to n_{Nb}, we have observed an intriguing temperature dependence of the SOC strength and the anisotropic magnetoresistance (MR) in the intermediate n_{Nb} region. These phenomena are associated with the temperature dependence of Landé g-factor and the change of the band structure, which is consistent with the result of density functional theory (DFT) calculation.

Electronic devices based on conventional semiconductors are facing the limit of evolution due to the huge consumption of energy, generation of excessive heat, monotonic functionality, and inextensible miniaturization. "Oxide-spintronics", based on a broad spectrum of electrical and magneto-electrical properties originating from the interplay between orbital and spin degrees of freedom combined with the strong correlation nature of electrons in transition-metal oxides, is considered as one of the promising solutions[1–8]. For the development of high-performance spintronic devices using oxide materials, an essential ingredient is a good spin channel, where the electron's spin can be manipulated at will within an infinitesimal energy and length scale.

Recently, observable effects of spin-orbit coupling (SOC) have been reported in various material systems, for example, topological insulators[9,10], two-dimensional materials[11], and some oxide materials such as LaAlO$_3$/SrTiO$_3$ (LAO/STO) heterostructure[12,13] and pyrochlore iridates (A_2Ir$_2$O$_7$, where A = yttrium and lanthanide element)[14–16]. In the former, a tunable and moderate strength SOC was reported while, in the latter, electrical and magnetic properties were reported to be dominated by the strong SOC. More recently, we found that a heavily Nb-doped SrTiO$_3$ (SrNb$_{0.2}$Ti$_{0.8}$O$_3$) epitaxial film grown on STO showed the strong SOC and the high carrier mobility – ideal characteristics for a good spin channel – which resulted in a large linear magnetoresistance (LMR)[17]. In this study, we have performed a systematic study on the magnetotransport properties of SrNb$_x$Ti$_{1−x}$O$_3$ films with varying Nb concentration (n_{Nb}) in the range of 2~20 at. % to find that the magnetotransport property is dominated by three-dimensional weak antilocalization (WAL)[18,19] and that the SOC strength is proportional to n_{Nb}. Furthermore, a few intriguing properties are also found, for example, non-monotonic temperature dependence of the SOC and anisotropy of MR in the intermediate n_{Nb} region.

Nb-concentration split SrTiO$_3$ (Nb:STO) films were fabricated at 700 °C in 10$^{−5}$ Torr of oxygen partial pressure using pulsed laser epitaxy (PLE). Laser (248 nm; IPEX 864, Lightmachinery, Nepean, Canada) fluence of 1.5 J/cm^2 and repetition rate of 5 Hz was used. SrTiO$_3$ and Sr(Nb$_{0.2}$Ti$_{0.8}$)O$_3$ targets were used to systematically modify

[1]Electronic Materials Research Center, Korea Institute of Science and Technology, Seoul, 02792, Korea. [2]Division of Nano & Information Technology, KIST School, Korea University of Science and Technology, Daejon, 34316, Korea. [3]Department of Physics, Sungkyunkwan University, Suwon, 16419, Korea. [4]Department of Materials Science and Engineering, Seoul National University, Seoul, 08826, Korea. Correspondence and requests for materials should be addressed to S.L. (email: slee_eels@kist.re.kr)
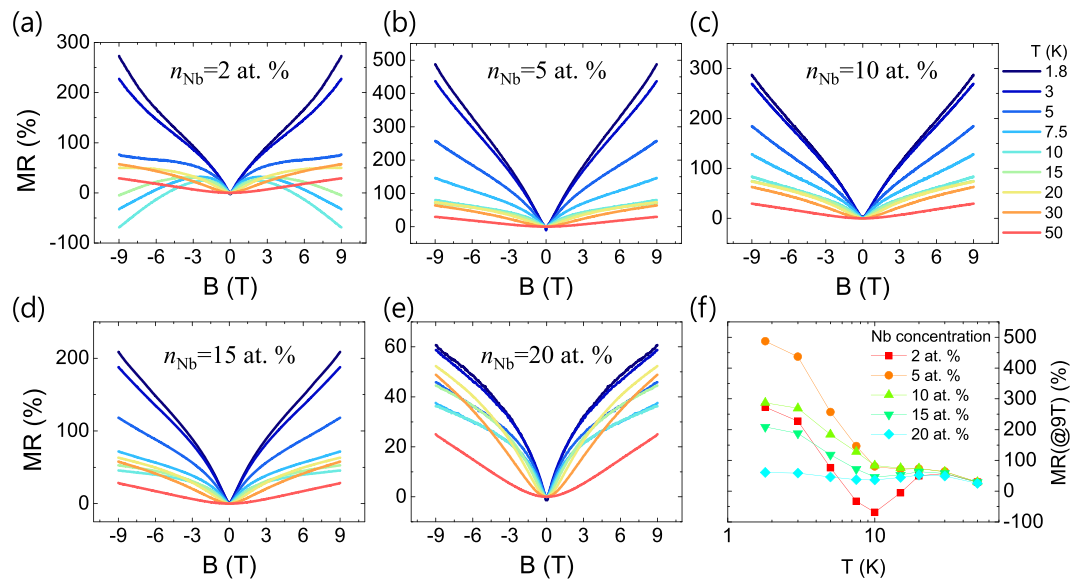
Figure 1. (**a~e**) Magnetoresistance (MR) vs. B curves of Nb:STO epitaxial films with varying Nb concentration (n_{Nb}) at various temperatures. The color code of all plots is same as that in (**c**). (**f**) Temperature dependence of MR at 9 T of Nb:STO films.

the Nb:STO concentration, by controlling the ablation ratio between the two targets within a unit cell thickness[20]. The advantage of using co-ablation of two targets instead of using Nb:STO solid solution target with different n_{Nb} was to avoid additional complexity and quality issues due to preparing distinctive targets. The thickness of the Nb:STO thin films was 16 ± 1 nm, as measured by X-ray reflectometry (XRR). The atomic structure and epitaxy relation of the thin films were characterized using high-resolution X-ray diffraction (XRD) (Rigaku, Smartlab) (in the Supplementary Information, Figure S1).

For the measurement of magnetotransport properties, a specimen was cut into 2(width) × 5(length) mm² and six electrical contacts were formed by indium. After wiring, the sample was inserted in a commercial cryogen-free cryostat (CMag Vari-9, Cryomagnetics Inc.) and the resistance was measured using a Source-Measure Unit (Keithley 2612A) and a nano-voltmeter (Keithley 2182).

For DFT calculation, Vienna Ab initio Simulation Package (VASP)[21] with PAW potentials. We employ HSE06 hybrid functional for the exchange-correlation functional and the energy cutoff of the plane-wave basis set to 450 eV for all calculation. For structural optimization, the $4 \times 4 \times 4$ Monkhorst-pack **k**-point sampling is used for primitive cell of SrTiO₃ and SrNbO₃ in cubic perovskite structure. The calculated lattice parameter of SrTiO₃ and SrNbO₃ are 3.883 Å and 4.017 Å, respectively, which are consistent with experimental values[22,23] with error less than 1%. We use the lattice parameter of 3.905 Å for the strained SrNbO₃ that corresponds to the experimental lattice of SrTiO₃. To calculate the density of states (DOS) of unstrained and strained SrNbO₃, we use $6 \times 6 \times 6$ Monkhorst-pack **k**-point sampling and tetrahedron method for Brillouin-zone integration. For the calculation of Nb:STO, we use the 130-atom supercell that one Ti atom is substituted by Nb which correspond to the doping concentration of 3.8 at %. For **k**-point sampling of defect cell, we use Γ-only k-point which corresponds to same **k**-point density compared to primitive cell. For DOS calculation of Nb:STO, we also use Γ-only **k**-point and Gaussian smearing for Brillouin-zone integration to reduce the computational cost.

Figure 1(a)~(e) show the magnetoresistance ($MR(B) = \frac{R(B) - R(0)}{R(0)} \times 100$ (%)) of Nb:STO films ($n_{Nb} = 2, 5, 10, 15, 20$ at. %) as a function of the applied magnetic field (B) at various temperature (T), where B is applied perpendicular to the film surface. A few intriguing features can be found. First, at low temperature ($T < 20$ K), the Nb:STO films show a sharp and linear MR vs. B curve at low field region ($|B| < \sim 2$ T) independent of n_{Nb}. This behavior is consistent with the LMR shown in heavily-doped Sr(Nb₀.₂Ti₀.₈)O₃ epitaxial films presented in our previous report[17]. Second, a lightly-doped Sr(Nb₀.₀₂Ti₀.₉₈)O₃ film has a peculiar T-dependence of the MR vs. B curve. In detail, in the temperature range from 7.5 to 15 K, MR decreases with increasing the strength of B in the high field region ($|B| > 2$ T) leading to a high negative MR of about -70 % at 10 K and 9 T. In contrast, the other samples do not show such a negative MR although they all show an anomalous behavior (minimum MR or change of slope) around 10 K as shown in Fig. 1(f). Similar behaviors, including the LMR, were observed in top-gated LaAlO₃/SrTiO₃ devices, where the sign change of MR was induced by electric field[12,24]. The authors explained those phenomena in terms of the change of the strength of WAL effect resulting from the change in the Rashba SOC constant by the top-gate bias[25]. The strength of WAL effect also depends on T, which is given by the sum of spin-orbit, spin-flip, and inelastic scatterings[18,19]. Therefore, the observed complex T-dependence of the MR vs. B curve can be associated with T-dependence of the WAL effect. In contrast to LaAlO₃/SrTiO₃ where the conduction is confined in the atomically-thin two dimensional (2D) channel, Nb:STO films are assumed to have three dimensional (3D) transport because their thickness is ~16 nm comparable to the mean free path. The 3D
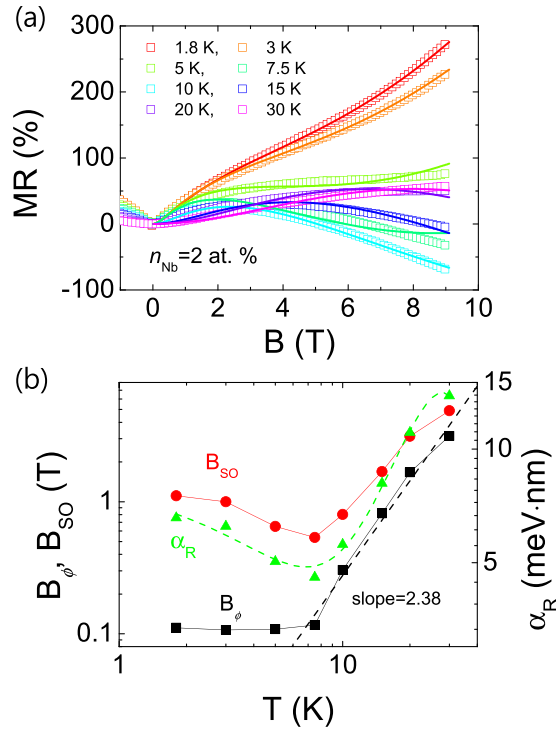
Figure 2. (**a**) MR vs. B curves of a Nb:STO film (n_{Nb} = 2 at. %) measured at various temperatures (symbol) together with fitting curves obtained by Eq. (3) (solid lines, see text). (**b**) Temperature dependence of the phase-coherence field (B_ϕ, black solid square), the spin-orbit field (B_{SO}, red solid circle), and the Rashba SOC constant (α_R, green solid triangle). A black dashed line is a linear fit to $B_\phi(T)$ curve for T above 7.5 K in the log-log scale, showing a power-law dependence of $B_\phi(T)$. A green dashed line is a fitting curve to the experimental $\alpha_R(T)$ assuming a quadratic dependence of Landé g-factor (see text).

WAL effect is described by Fukuyama-Hoshino (F-H) model[26–28], where MR is given by the following equations (1) and (2).

$$\frac{\Delta\rho_{WAL}(B)}{\rho(0)^2} = \frac{e^2}{2\pi^2 h}\sqrt{\frac{2\pi eB}{h}}\left[\frac{1}{2}f_3\left(\frac{B}{B_\phi}\right) - \frac{3}{2}f_3\left(\frac{B}{B_2}\right)\right]$$

(1)

$$f_3(y) = \sum_{n=0}^{\infty}\left[2\left(n+1+\frac{1}{y}\right)^{\frac{1}{2}} - 2\left(n+\frac{1}{y}\right)^{\frac{1}{2}} - \left(n+\frac{1}{2}+\frac{1}{y}\right)^{-\frac{1}{2}}\right]$$

(2)

In Eq. (1), e and h are the charge of an electron and Planck's constant, respectively. And, $B_\phi = B_i + 2B_S$ and $B_2 = B_i + \frac{2}{3}B_S + \frac{4}{3}B_{SO}$, where $B_x = \frac{\hbar}{4eD\tau_x}$ and τ_xs (where $x = i$, S, and SO) are the characteristic time for the inelastic, spin-flip, and spin-orbit scattering, respectively. And, $\hbar$ and D are the reduced Planck's constant ($= h/2\pi$) and diffusion coefficient of electron in Nb:STO, respectively.

In Fig. 2(a), T-dependent MR vs. B curves of a Nb:STO film (n_{Nb} = 2 at. %) are replotted along with the respective fitting curves, which are given by the following equation (Eq. (3))[29,30].

$$MR(B, T) = C * R(0, T) * \frac{e^2}{2\pi^2 h}\sqrt{\frac{2\pi eB}{h}}\left[\frac{1}{2}f_3\left(\frac{B}{B_\phi(T)}\right) - \frac{3}{2}f_3\left(\frac{B}{B_2(T)}\right)\right] + k\left(\frac{B}{R(0, T)}\right)^2$$

(3)

The first and the second term originate from the WAL and the classical orbital motion, respectively, where the latter is assumed to follow the Kohler's rule[31] with k being a constant independent of T. C is a constant which depends only on the geometry of the device and $R(0, T)$ is the resistance under zero magnetic field at various T. Consequently, two fitting parameters, B_ϕ and B_2, are used except for the curve at 1.8 K, at which k is also used as a fitting parameter and kept constant for the other temperatures. As shown in Fig. 2(a), it is found that Eq. (3) well reproduces the measured MR(B) curves in the investigated temperature range (1.8~30 K) even though the observed T-dependence is rather complex. The obtained values of B_ϕ and B_{SO} are plotted as a function of T in Fig. 2(b), which are in the similar range to those of top-gated LaAlO$_3$/SrTiO$_3$ devices, 0.1 T < B_{SO} < 10 T depending on the top-gate bias and 0.05 T < B_ϕ < 0.4 T at 1.5 K[12,24]. Above 7.5 K, B_ϕ increases with T faster than
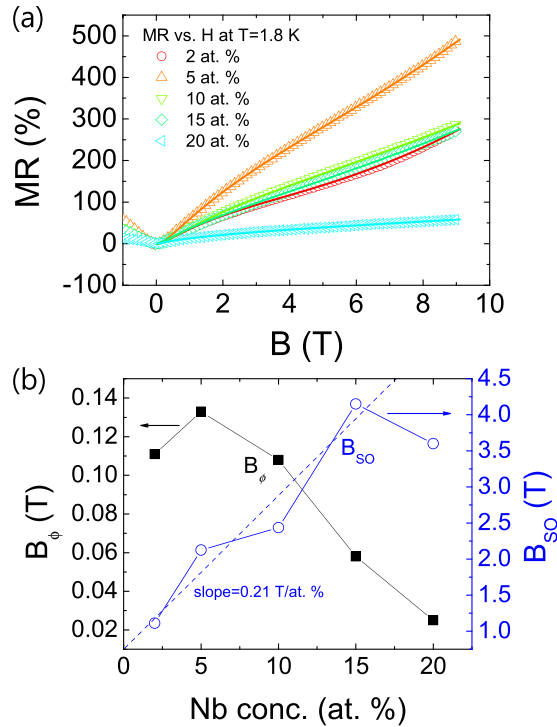
Figure 3. (**a**) MR vs. B curves of a Nb:STO films with varying n_{Nb} measured at 1.8 K (symbol) together with fitting curves obtained by Eq. (3) (solid lines, see text). (**b**) B_ϕ (black solid square) and B_{SO} (blue open circle) as a function of n_{Nb}.

B_{SO} indicating that the inelastic scattering by phonon is as important as SOC above ~15 K. T-dependence of B_ϕ is shown to follow a power-law behavior ($B_\phi \sim T^p$) for $T > 7.5$ K as shown in the linear fit in Fig. 2(b). According to ref.[32], p is expected to be 3/2 for electron-electron (e-e) scattering, 2 for inelastic scattering by transverse phonon, and 3 for inelastic scattering for longitudinal phonon, respectively. In Fig. 2(b), p is estimated to be ~2.38 indicating that, above 7.5 K, the phase relaxation is dominated by the phonon scattering with mixed contributions from the transverse and longitudinal phonons.

Below 7.5 K, B_{SO} is much higher than B_ϕ, indicating that SOC dominates the scattering in that temperature range. An intriguing feature in Fig. 2(b) is the appearance of a minimum B_{SO} at 7.5 K, which reminds of the aforementioned anomalous behavior of MR around 10 K presented in Fig. 1(f). Therefore, it seems to imply that the T-dependence of B_{SO} is closely related to the "10 K anomaly" of MR.

As a possible scenario to explain the T-dependence of B_{SO}, we consider the T-dependent Rashba constant (α_R) originating from the T-dependence of Landé g-factor (g). In detail, assuming that the spin relaxation is dominated by the D'Yakonov-Perel (D-P) mechanism, B_{SO} can be expressed in terms of α_R by $B_{SO} = \frac{\alpha_R^2 m^{*2}}{e\hbar^3}$, where m^* is the effective mass of an electron[27,33]. Figure 2(b) also shows the calculated $\alpha_R(T)$ (green triangle symbol) using the above relation and the known value of $m^*(=7.5m_0, m_0 =$ the rest mass of an electron) in Nb:STO, as $m^* = (7.3 \sim 7.7)m_0$ was previously reported[34]. In addition, neglecting the effect of the band structure on SOC, α_R is expressed in terms of g as $\alpha_R = g(1 - g)\frac{\pi e\hbar^2 \varepsilon}{4m^2 c^2}$, where ε and c are the electric field generated by the asymmetric structure and the speed of light, respectively[35]. In previous studies[36–39], it has been shown that g depends on T, implying that both α_R and B_{SO} should also depend on T. With the specific form of $g(T)$ depending on the material, the observed $\alpha_R(T)$ is well reproduced by an assumption of a quadratic T-dependence of g ($g(T) = g_0 + g_1 T + g_2 T^2$) similar to CdTe case[36], as shown by the fitting curve (green dashed line in Fig. 2(b)). It implies that the anomalous behavior of MR(T) and $\alpha_R(T)$ is associated with the T-dependence of g although the specific form of $g(T)$ of Nb:STO needs to be measured for confirmation. As another possibility, it might be associated with the unknown phase of heavily-doped Nb:STO epitaxial films under strain. In our previous work, it was found that a heavily doped Nb:STO film ($n_{Nb} = 20$ at. %) showed an upturn in resistivity and magnetic moment below 10 K as well as a local minimum in Hall carrier density around 10 K[17]. Further studies are needed to clarify the origin of the phenomenon.

With a plausible explanation of the MR vs. B behavior using the above model (Eq. (3)), MR vs. B curves of Nb:STO films with varying n_{Nb} at 1.8 K are plotted in Fig. 3(a) to investigate the n_{Nb}-dependence of SOC. The respective fitting curves are also plotted, providing the information of the dependence of B_ϕ and B_{SO} on n_{Nb} as shown in Fig. 3(b). For all doping concentrations, it is found that B_{SO} is much higher than B_ϕ indicating that SOC is the dominant scattering mechanism in Nb:STO epitaxial films in the low temperature region. Except at $n_{Nb} = 20$ at. %, it is found that B_{SO} linearly increases with n_{Nb} consistent with an expectation, since SOC is expected to be higher for a compound composed of elements with the higher atomic number (Z) elements ($Z_{Nb} = 41$ compared
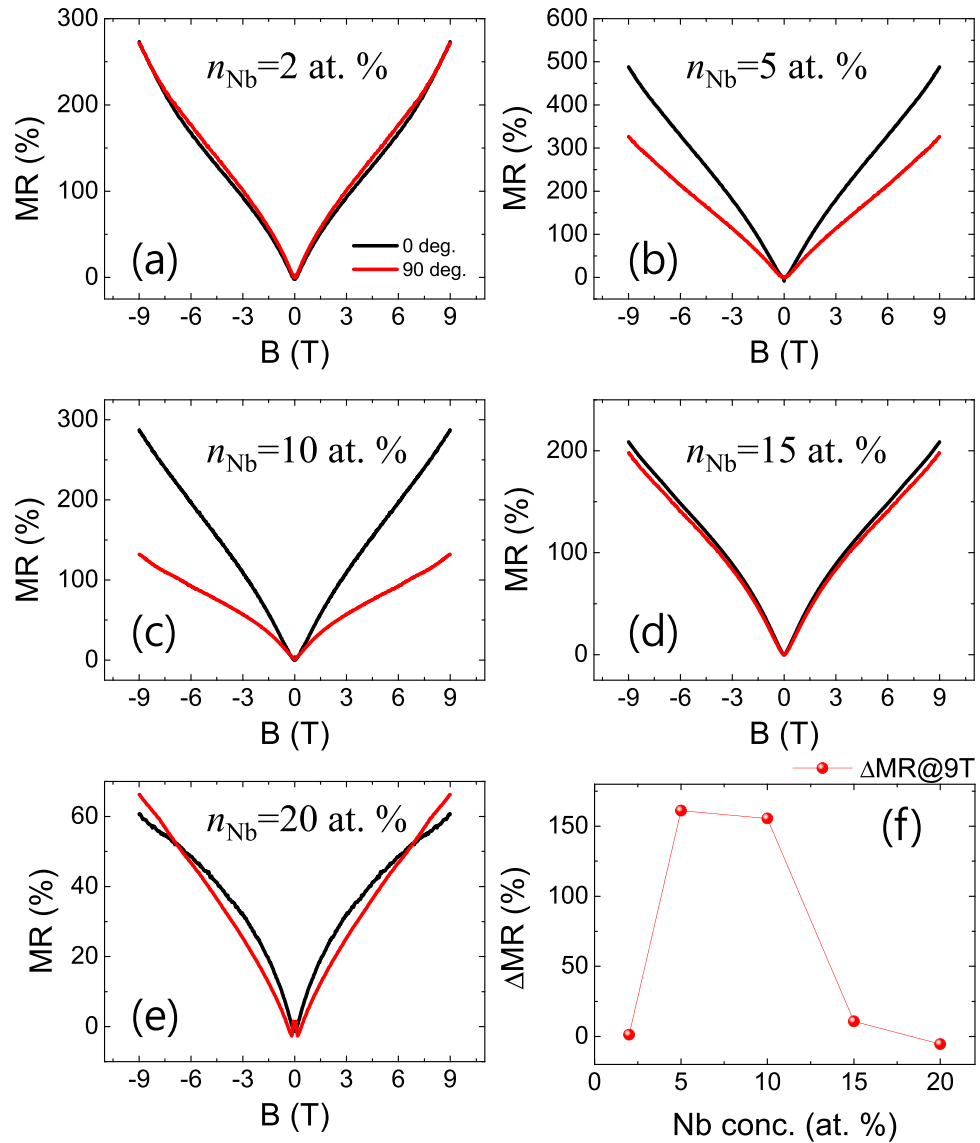
Figure 4. (**a~e**) MR vs. *B* curves of Nb:STO epitaxial films at 1.8 K under the out-of-plane (0 deg., black) and the in-plane (90 deg., red) magnetic field. (**f**) Difference in MR (ΔMR = MR_{perp}-MR_{para}) at 9 T as a function of n_{Nb}.

to Z_{Ti} = 22). As for the origin of a decrease in B_{SO} and a drastic reduction in MR at n_{Nb} = 20 at. %, we suggest that a new band might participate in the carrier transport as the Fermi level (E_F) increases over a threshold. A few evidences supporting this explanation are presented in the following.

In Fig. 4(a)~(e), MR vs. *B* curves of Nb:STO films at 1.8 K are presented with *B* oriented out-of-plane (MR_{perp}, 0 deg.) and in-plane (MR_{para}, 90 deg.), respectively. For the in-plane MR, the current is still applied perpendicular to *B*. The difference of MR (ΔMR = MR_{perp}-MR_{para} at 9 T) is plotted as a function of n_{Nb} in Fig. 4(f). It is interesting to note that a large anisotropy of MR is found for n_{Nb} = 5 at. % and n_{Nb} = 10 at. % samples whereas a negligibly small anisotropy is observed for the others. This observation seems to imply a change in the shape of the conduction band depending on n_{Nb}. The band structure of n_{Nb} = 2, 15, and 20 at. % samples should be symmetric along k_x (or k_y) and k_z direction in *k*-space while that of n_{Nb} = 5 and 10 at. % samples is expected to be asymmetric. This change in the shape of the conduction band depending on n_{Nb} might be associated with the crystal field splitting of Nb *d*-orbitals. It was known that the conduction band of Nb:STO is composed of degenerate Ti *d*-orbitals and Nb *d*-orbitals[40–42]. Since the Nb:STO film epitaxially grown on STO is strained as shown in XRD data (see Figure S1 in the Supplementary Information), *d*-orbitals of Nb atom are exerted by the crystal field possibly resulting in the splitting of energy levels. Consequently, the orbital-resolved conduction band structure of a Nb:STO film is expected to be similar to that seen in Fig. 5(a). For low n_{Nb}, if E_F is located within the overlap between degenerate Ti-*d* bands and Nb-$d_{x^2-y^2}$ band, the transport should be symmetric along k_x (or k_y) and k_z direction. Since Nb substituting Ti produces electron carriers[43,44], E_F increases with n_{Nb}. As n_{Nb} increases, E_F enters the region where the conduction band is contributed mainly from Nb-$d_{x^2-y^2}$ band resulting in 2D trans-
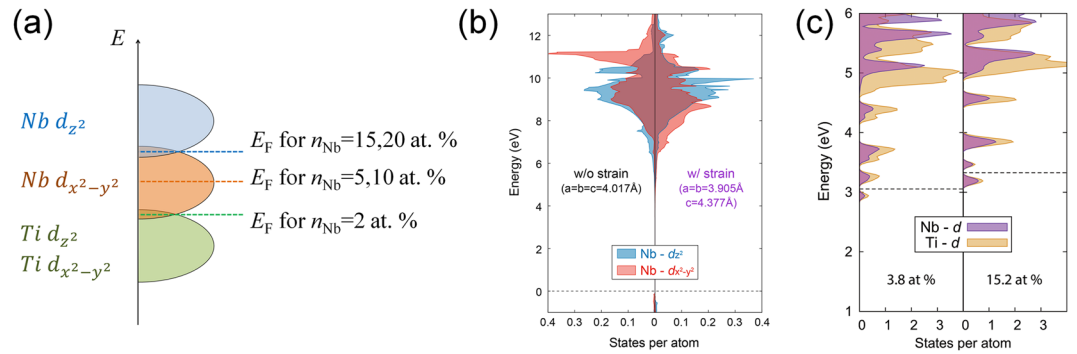
Figure 5. (a) A schematic illustration of the orbital-resolved band structure of Nb-doped $SrTiO_3$ epitaxial film grown on $SrTiO_3$. (b) Orbital-resolved band structure of unstrained $SrNbO_3$ film (left panel, $a = 4.017$ Å) and strained $SrNbO_3$ film with the in-plane lattice constant same as $SrTiO_3$ (right panel, $a = 3.905$ Å). Dashed-line shows the position of valence band maximum. (c) Orbital-resolved band structure of $Sr(Nb_xTi_{1-x})O_3$ for x = 3.8 at % and 15.2 at %. The E_F of each model is shown as dashed lines.

port nature. As E_F increases further, Nb-d_{z^2} starts to contribute to the conduction band again making the conduction along k_z direction significant. This picture can naturally explain the change of the MR anisotropy depending on n_{Nb}.

To verify the assumed band structure, we have performed the orbital-resolved band calculation using density functional theory (DFT), which is shown in Fig. 5(b). For simplicity, we have calculated the band structure of $SrNbO_3$, which can provide qualitative but essential information on the change of the band structure on doping Nb in $SrTiO_3$. The left and right panels show the partial density of states (PDOS) for an unstrained $SrNbO_3$ ($a = 4.017$ Å)[22,45] and a strained film epitaxially grown on $SrTiO_3$ ($a = 3.905$ Å)[23], respectively. Comparing with the unstrained $SrNbO_3$, it is found that Nb-$d_{x^2-y^2}$ band moves to lower energy whereas Nb-d_{z^2} band moves to higher energy consistent with our expectation described above. To compare the relative position of Nb-d in Nb:STO, we also calculate the PDOS of Nb:STO ($n_{Nb} = 3.8$ at % and 15.2 at %) as shown in Fig. 5(c). It is shown that the position of Nb-d composing the conduction band is right above the position of Ti-d as we assumed in Fig. 5(a). Comparing results of different n_{Nb}, it is also shown that E_F increases with n_{Nb}. Therefore, we believe that the crystal-field splitting of the Nb d-bands in Nb:STO films is associated with the observed change in the anisotropy of MR. As alternative explanation, the interaction of d-electrons under a strong SOC should be addressed because it was reported to be important in material systems including transition metal elements[46].

In summary, we have investigated magnetotransport properties of epitaxial Nb:STO thin films to find the effect of Nb on the SOC strength. The magnetotransport properties are well described by the F-H model describing 3D WAL and the estimated SOC strength is found to be proportional to n_{Nb}. Furthermore, a few intriguing phenomena are presented, non-monotonic temperature dependence of the SOC strength and anisotropy of MR in the intermediate n_{Nb} region, which might be explained in terms of the temperature dependence of the g-factor and the change in band structure with n_{Nb}. This result demonstrates that the epitaxial Nb:STO film basically possesses the strong SOC, whose strength can be controlled by n_{Nb}. We believe that these results not only provide a material platform to study the interplay between SOC and strong correlation, which is an interesting subject in condensed-matter physics, but also enable us to design advanced spintronic devices and other novel functional devices combining the strong SOC and other versatile functionalities of strongly-correlated oxides.

References

1. Wolf, S. A. *et al.* Spintronics: A Spin-Based Electronics Vision for the Future. *Science* **294**, 1488–1495, https://doi.org/10.1126/science.1065389 (2001).
2. Ziese, M. & Thornton, M. J. *Spin Electronics.* (Springer Berlin Heidelberg, 2001).
3. Ramirez, A. P. Oxide Electronics Emerge. *Science* **315**, 1377–1378, https://doi.org/10.1126/science.1138578 (2007).
4. Mannhart, J. & Schlom, D. G. Oxide Interfaces—An Opportunity for Electronics. *Science* **327**, 1607–1611, https://doi.org/10.1126/science.1181862 (2010).
5. Lorenz, M. *et al.* The 2016 oxide electronic materials and oxide interfaces roadmap. *Journal of Physics D: Applied Physics* **49**, 433001 (2016).
6. Hwang, H. Y. *et al.* Emergent phenomena at oxide interfaces. *Nat Mater* **11**, 103–113 (2012).
7. Ngai, J. H., Walker, F. J. & Ahn, C. H. Correlated Oxide Physics and Electronics. *Annual Review of Materials Research* **44**, 1–17, https://doi.org/10.1146/annurev-matsci-070813-113248 (2014).
8. Bibes, M. & Barthelemy, A. Oxide Spintronics. *IEEE Transactions on Electron Devices* **54**, 1003–1023, https://doi.org/10.1109/TED.2007.894366 (2007).
9. Yang, M. & Liu, W.-M. The d-p band-inversion topological insulator in bismuth-based skutterudites. *Scientific Reports* **4**, 5131, https://doi.org/10.1038/srep05131, https://www.nature.com/articles/srep05131#supplementary-information (2014).
10. Jin, H. *et al.* High mobility, large linear magnetoresistance, and quantum transport phenomena in Bi2Te3 films grown by metallo-organic chemical vapor deposition (MOCVD). *Nanoscale* **7**, 17359–17365, https://doi.org/10.1039/C5NR05491E (2015).
11. Krasovskii, E. E. Spin–orbit coupling at surfaces and 2D materials. *Journal of Physics: Condensed Matter* **27**, 493001 (2015).
12. Caviglia, A. D. *et al.* Tunable Rashba Spin-Orbit Interaction at Oxide Interfaces. *Physical Review Letters* **104**, 126803 (2010).
13. Herranz, G. *et al.* Engineering two-dimensional superconductivity and Rashba spin–orbit coupling in LaAlO3/SrTiO3 quantum wells by selective orbital occupancy. **6**, 6028, https://doi.org/10.1038/ncomms7028, http://dharmasastra.live.cf.private.springer.com/articles/ncomms7028#supplementary-information (2015).

14. Pesin, D. & Balents, L. Mott physics and band topology in materials with strong spin-orbit interaction. *Nat Phys* **6**, 376–381, http://www.nature.com/nphys/journal/v6/n5/suppinfo/nphys1606_S1.html (2010).
15. Cui, Q. *et al.* Slater Insulator in Iridate Perovskites with Strong Spin-Orbit Coupling. *Physical Review Letters* **117**, 176603 (2016).
16. Wan, X., Turner, A. M., Vishwanath, A. & Savrasov, S. Y. Topological semimetal and Fermi-arc surface states in the electronic structure of pyrochlore iridates. *Physical Review B* **83**, 205101 (2011).
17. Jin, H. *et al.* Large linear magnetoresistance in heavily-doped Nb:SrTiO$_3$ epitaxial thin films. *Scientific Reports* **6**, 34295, https://doi.org/10.1038/srep34295, https://www.nature.com/articles/srep34295#supplementary-information (2016).
18. Altshuler, B. L., Khmel'nitzkii, D., Larkin, A. I. & Lee, P. A. Magnetoresistance and Hall effect in a disordered two-dimensional electron gas. *Physical Review B* **22**, 5142–5153 (1980).
19. Datta, S. *Electronic Transport in Mesoscopic Systems*. (Cambridge University Press, 1997).
20. Choi, W. S., Lee, S., Cooper, V. R. & Lee, H. N. Fractionally δ-Doped Oxide Superlattices for Higher Carrier Mobilities. *Nano Letters* **12**, 4590–4594, https://doi.org/10.1021/nl301844z (2012).
21. Kresse, G. & Hafner, J. Ab initio. *Physical Review B* **47**, 558–561 (1993).
22. Turzhevsky, S. A., Novikov, D. L., Gubanov, V. A. & Freeman, A. J. Electronic structure and crystal chemistry of niobium oxide phases. *Physical Review B* **50**, 3200–3208 (1994).
23. Dawber, M. *et al.* Unusual Behavior of the Ferroelectric Polarization in PbTiO$_3$/SrTiO$_3$ Superlattices. *Physical Review Letters* **95**, 177601 (2005).
24. Hurand, S. *et al.* Field-effect control of superconductivity and Rashba spin-orbit coupling in top-gated LaAlO$_3$/SrTiO$_3$ devices. *Scientific Reports* **5**, 12751, https://doi.org/10.1038/srep12751, https://www.nature.com/articles/srep12751#supplementary-information (2015).
25. Yu, A. B. & Rashba, E. I. Oscillatory effects and the magnetic susceptibility of carriers in inversion layers. *Journal of Physics C: Solid State Physics* **17**, 6039 (1984).
26. Fukuyama, H. & Hoshino, K. Effect of Spin-Orbit Interaction on Magnetoresistance in the Weakly Localized Regime of Three-Dimensional Disordered Systems. *Journal of the Physical Society of Japan* **50**, 2131–2132, https://doi.org/10.1143/JPSJ.50.2131 (1981).
27. Hikami, S., Larkin, A. I. & Nagaoka, Y. Spin-Orbit Interaction and Magnetoresistance in the Two Dimensional Random System. *Progress of Theoretical Physics* **63**, 707–710, https://doi.org/10.1143/ptp.63.707 (1980).
28. Hu, J., Liu, J. Y. & Mao, Z. Q. Spin–orbit coupling and weak antilocalization in the thermoelectric material β-K$_2$Bi$_8$Se$_{13}$. *Journal of Physics: Condensed Matter* **26**, 095801 (2014).
29. Kawabata, A. Theory of Negative Magnetoresistance I. Application to Heavily Doped Semiconductors. *Journal of the Physical Society of Japan* **49**, 628–637, https://doi.org/10.1143/JPSJ.49.628 (1980).
30. B. L. Altshuler A. G. A., A. I. Larkin, & D. E. Khmelnitskii. Anomalous magnetoresistance in semiconductors. *Sov. Phys. JETP* **54** (1981).
31. Ziman, J. M. *Electrons and Phonons: The Theory of Transport Phenomena in Solids*. (OUP Oxford, 1960).
32. Lin, J. J. & Bird, J. P. Recent experimental studies of electron dephasing in metal and semiconductor mesoscopic structures. *Journal of Physics: Condensed Matter* **14**, R501 (2002).
33. Dyakonov, M. & Perel, V. Spin relaxation of conduction electrons in noncentrosymmetric semiconductors. *Soviet Physics Solid State, Ussr* **13**, 3023–3026 (1972).
34. Ohta, S., Nomura, T., Ohta, H. & Koumoto, K. High-temperature carrier transport and thermoelectric properties of heavily La- or Nb-doped SrTiO$_3$ single crystals. *Journal of Applied Physics* **97**, 034106, https://doi.org/10.1063/1.1847723 (2005).
35. Zhang, L. *et al.* Sensitively Temperature-Dependent Spin–Orbit Coupling in SrIrO$_3$ Thin Films. *Journal of the Physical Society of Japan* **83**, 054707, https://doi.org/10.7566/JPSJ.83.054707 (2014).
36. Oestreich, M. *et al.* Temperature and density dependence of the electron Land\'e g factor in semiconductors. *Physical Review B* **53**, 7911–7916 (1996).
37. Pidgeon, C. R. *et al.* in *Narrow Gap Semiconductors 2007: Proceedings of the 13th International Conference, 8–12 July, 2007, Guildford, UK* (eds Murdin, Ben & Clowes, Steve) 27–29 (Springer Netherlands, 2008).
38. Buß, J. H., Schupp, T., As, D. J., Hägele, D. & Rudolph, J. Temperature dependence of the electron Landé g-factor in cubic GaN. *Journal of Applied Physics* **118**, 225701, https://doi.org/10.1063/1.4937128 (2015).
39. Zhou, R. *et al.* Temperature dependence of effective g factor in diluted magnetic semiconductor (Ga,Mn)As. *Journal of Applied Physics* **103**, 053901, https://doi.org/10.1063/1.2842400 (2008).
40. Zhang, Y. *et al.* Thermoelectric phase diagram of the SrTiO3–SrNbO3 solid solution system. *Journal of Applied Physics* **121**, 185102, https://doi.org/10.1063/1.4983359 (2017).
41. Wan, D. Y. *et al.* Electron transport and visible light absorption in a plasmonic photocatalyst based on strontium niobate. *Nature Communications* **8**, 15070, https://doi.org/10.1038/ncomms15070, https://www.nature.com/articles/ncomms15070#supplementary-information (2017).
42. Chen, C. *et al.* Atomic and electronic structure of the SrNbO$_3$/SrNbO$_{3.4}$ interface. *Applied Physics Letters* **105**, 221602, https://doi.org/10.1063/1.4902970 (2014).
43. Tomio, T. & Miki, H. Control of electrical conductivity in laser deposited SrTiO$_3$ thin films with Nb doping. *Journal of Applied Physics* **76**, 5886, https://doi.org/10.1063/1.358404 (1994).
44. Blennow, P., Hagen, A., Hansen, K. K., Wallenberg, L. R. & Mogensen, M. Defect and electrical transport properties of Nb-doped SrTiO$_3$. *Solid State Ionics* **179**, 2047–2058, https://doi.org/10.1016/j.ssi.2008.06.023 (2008).
45. Majid, A. & Lee, Y. S. in *Proceedings of the 2nd International Conference on Interaction Sciences: Information Technology, Culture and Human* 175–183 (ACM, Seoul, Korea, 2009).
46. Yang, M., Zhang, X.-L. & Liu, W.-M. Tunable topological quantum states in three- and two-dimensional materials. *Frontiers of Physics* **10**, 161–176, https://doi.org/10.1007/s11467-015-0463-3 (2015).

Acknowledgements

Author Contributions

S.L. designed and conceived the experiments with help from S.W.C. and M.L. Growth of Nb:STO films and the analysis of XRD patterns were done by S.W. and W.S.C. S.W.C. and M.L. performed the low-temperature magnetotransport measurement. The analysis of magnetotransport data was done by S.W.C. and S.L., K.Y. and S.H. performed the DFT. calculation. All authors discussed the data and participated in the writing of the manuscript.

Additional Information

Supplementary information accompanies this paper at https://doi.org/10.1038/s41598-018-23967-2.

Competing Interests: The authors declare no competing interests.

Publisher's note: Springer Nature remains neutral with regard to jurisdictional claims in published maps and institutional affiliations.